

Surface Magnetic Ordering: A Spin-Polarized Photoemission Study of Thin Films of Gd

P. Dowben and C. Waldfried (University of Nebraska), E. Vescovo (NSLS)

Perhaps the most remarkable example of the uniqueness of surface magnetic properties is the condition of magnetically ordered surfaces at temperatures where the bulk material is paramagnetic. This is well documented for the rare-earth elements. An enhanced magnetization has also been proposed for chromium surfaces, and the face centered iron phase. This property of the rare earth surfaces is a dramatic example of the different magnetic, as well as electronic, properties that exist at surfaces, as noted, for example, in the recently completed review chapter on the surface magnetism of the rare earth metals by P.A. Dowben *et al*^[1].

C. Waldfried and coworkers from the Dowben group have utilized their previous experimental discovery of a localized surface state on the Gd(0001) surface to probe the origin of the different magnetic properties of the surfaces of both “unstrained” and 4% expansively strained gadolinium films. They find that the occupied *bulk* Gd 5d/6s bands for both strained and unstrained Gd exhibit a Stoner-like exchange splitting consistent with theory^[2]. However, the strained Gd(0001) surface exhibits a mixture of Stoner-like magnetism and spin-mixing behavior^[1], with more rigid band ferromagnetism than the unstrained surface.

During the past year a considerable amount of work focused on a detailed study of the band structure of the 4%-strained Gd(0001) surface using spin polarized electron spectroscopy^[3]. An important result of these measurements is that they show very

clearly that the exchange splitting, and by extension perhaps the magnetic coupling, is electron wave vector dependent as seen in **Figure M-1**. Finite-temperature many-body band-structure-calculations^[2] predict this result, but the extent of this wave vector dependence is surprising. Consistent with the enhanced magnetization of the surface, the exchange splitting and wave vector dependence of the surface is different from the bulk, being dominated by the more localized band structure of the surface.

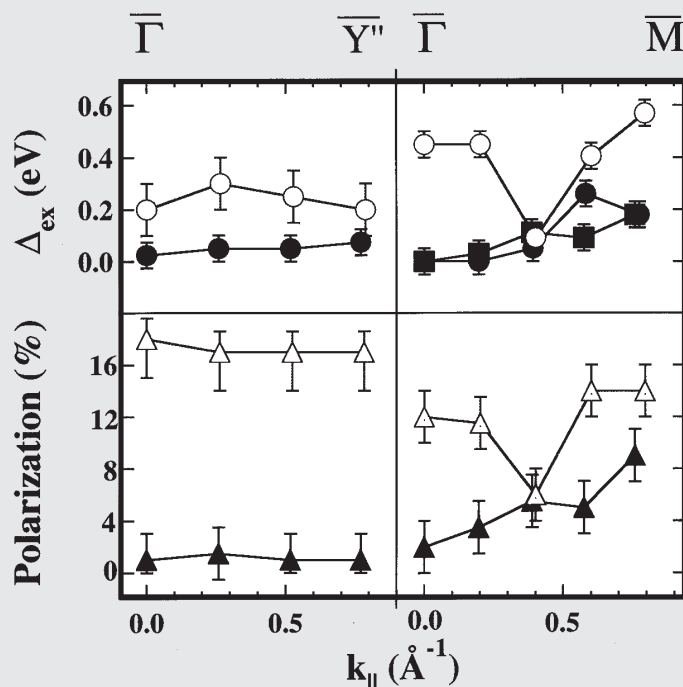


Figure M-1: Wave vector dependence of the exchange splitting and polarization of the Gd surface state (open symbols) and bulk states (filled symbols) for strained Gd(1012) (4ML - left) and strained Gd(0001) (40 ML - right).

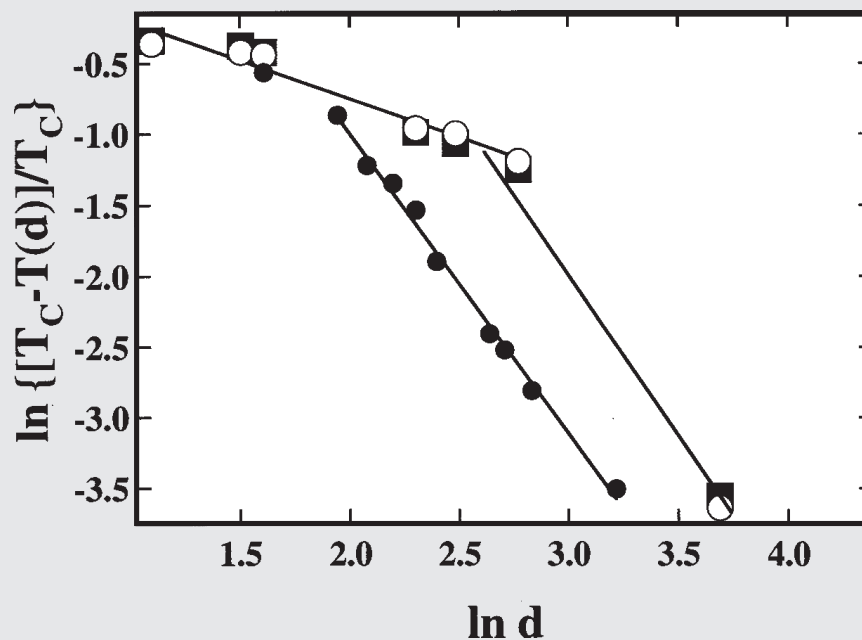


Figure M-2: The logarithm of the reduced Curie temperature for strained gadolinium surface (open circles) and bulk (closed squares) are compared to unstrained gadolinium (closed circles) as a function of film thickness.

A second very important result is that there is direct evidence that the surface Gd 5d exchange splitting, and thus the magnetic moment, is enhanced over the bulk particularly for the expansively strained Gd(0001) surface. The observed surface Curie temperature of these films is 370 K and is much higher than the bulk Curie temperature for expansively strained Gd(0001). Both of these temperatures are much higher than the generally accepted bulk Curie temperature of gadolinium of 293 K. It is very clear that the surface plays the role of an “actor” not a “spectator” and will influence finite size scaling behavior in the ultra-thin film limit^[3]. This is indicated in Figure M-2. ■

[1] P.A. Dowben, D.N. McIlroy and Dongqi Li, “Surface Magnetism of the Rare Earth Metals”, Handbook on the Physics and Chemistry of the Rare Earths, Edited by K.A. Gschneidner and Leroy Eyring, (Chapt. 159) **24**, 1, (1996).

[2] W. Nolting, T. Dambeck and G. Borstel, *Z. Phys. Rev. B* **94**, 409, (1994).

[3] C. Waldfried, D. Welipitiya, T. McAvoy, E. Vescovo and P.A. Dowben, “Wave Vector Dependent Exchange Splitting in a Local Moment System”, submitted to *Phys. Rev. Lett.*

C. Waldfried, T. McAvoy, D. Welipitiya, P.A. Dowben, and E. Vescovo, “The Influence of Enhanced Surface Magnetism on Finite Size Scaling”, submitted to *Europhys. Lett.*

First Observation of Half-Metallic Behavior: A Spin-Polarized Photoemission Study of Thin Films of $\text{La}_{0.7}\text{Sr}_{0.3}\text{MnO}_3$

J.-H. Park, E. Vescovo, and H.-J. Kim (NSLS)

As mentioned above, a considerable amount of experimental work at U5UA during 1997 was devoted to the study of the electronic structure of a thin film of $\text{La}_{0.7}\text{Sr}_{0.3}\text{MnO}_3$. This material belongs to the class of manganese perovskites, derived from the antiferromagnetic insulating parent-compound LaMnO_3 by partial substitution of La with Sr atoms. As is well known, with increasing temperature this material undergoes a complex phase transition from a metallic-ferromagnetic phase at low temperatures to an insulating-paramagnetic phase at high temperature ($T_c \sim 350$ K). This link between metallic character and ferromagnetic behavior, as opposed to insulating and antiferromagnetism, seems to be a quite general characteristic of transition metal oxides^[1] and has been explained, at least in some cases, by the so-called double exchange mechanism^[2]. According to this model, substituting divalent Sr atoms for trivalent La ones forces a corresponding number of Mn ions to become tetravalent: the system is now a mixed-valent compound

in which both Mn^{3+} (as in LaMnO_3) and Mn^{4+} ions are present. The conduction can then be sustained (at no cost, in the ferromagnetic system) by electron hopping from a Mn^{3+} to a neighboring Mn^{4+} site (the two configurations $\text{Mn}^{3+}\text{-O}^{2-}\text{-Mn}^{4+}$ and $\text{Mn}^{4+}\text{-O}^{2-}\text{-Mn}^{3+}$ being obviously degenerate). This transport mechanism is mediated by the O^{2-} ions, which permit a “double exchange” in which an electron is exchanged between a $3d$ orbital of the Mn^{3+} ion and an $\text{O } 2p$ electron, while at the same time another electron is exchanged from the $\text{O } 2p$ to the Mn^{4+} ions. However, owing to the strong on-site Mn exchange interaction, this hopping is allowed only if the two neighboring Mn ions are ferromagnetically aligned: i.e. the system can become metallic only if it also orders ferromagnetically. A very important consequence of this conduction mechanism is that this system should then have charge-carriers all with the same (majority) spins, i.e. it should be a perfect half-metallic system displaying 100% spin-polarization at the Fermi level. In Figure M-3, the metal-to-insulator transition of

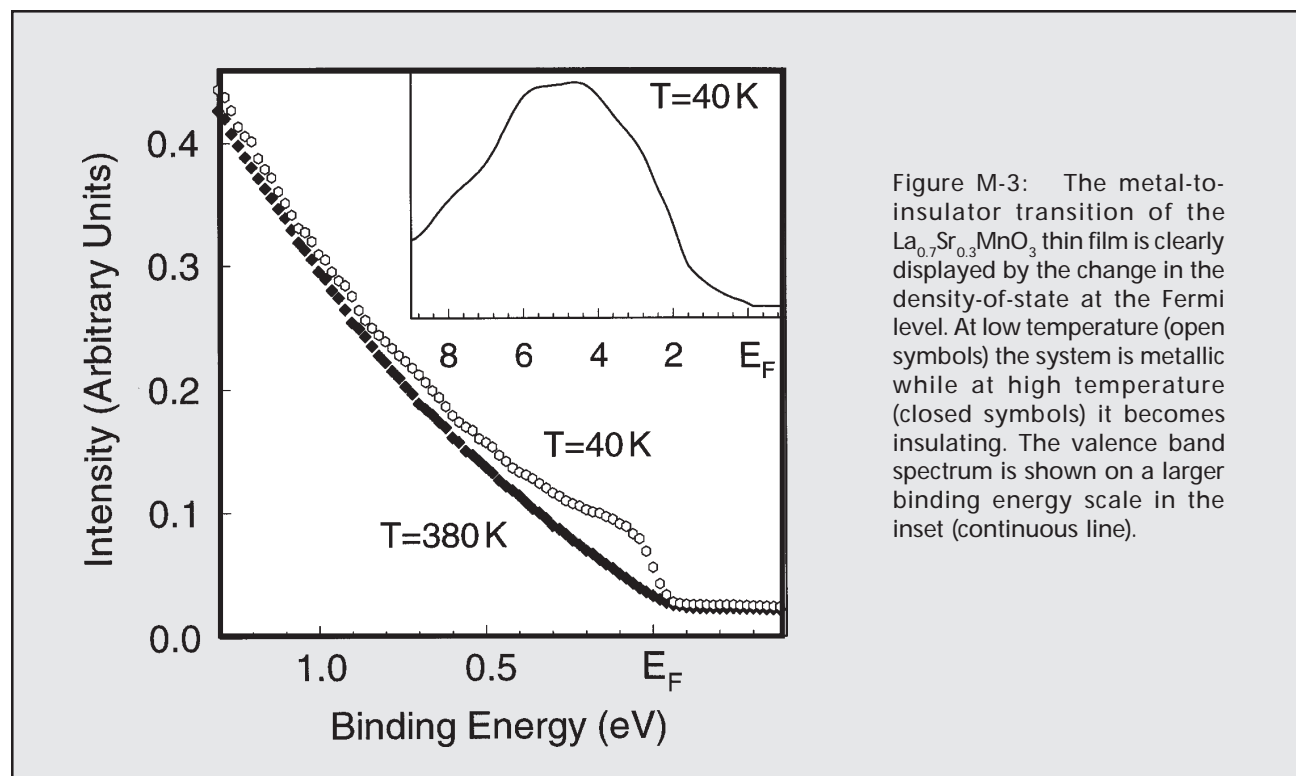


Figure M-3: The metal-to-insulator transition of the $\text{La}_{0.7}\text{Sr}_{0.3}\text{MnO}_3$ thin film is clearly displayed by the change in the density-of-state at the Fermi level. At low temperature (open symbols) the system is metallic while at high temperature (closed symbols) it becomes insulating. The valence band spectrum is shown on a larger binding energy scale in the inset (continuous line).

$\text{La}_{0.7}\text{Sr}_{0.3}\text{MnO}_3$ is clearly displayed: the density-of-state at the Fermi level disappears with increasing temperature. **Figure M-4** instead shows the spin-resolved spectrum of the valence band in a region very close to the Fermi level when the system is kept at low temperature, i.e. in its ferromagnetic-metallic phase. Unambiguously, the predicted 100% spin-polarization is observed close to the Fermi level. The proof of the existence of half-metallic systems^[3] is not only important from the fundamental point of view but also has important implications for technological applications. Indeed, the realization of an half-metallic system also implies, for example, the realization of a 100% spin-polarized electron source or the realization of a perfect spin-filter. For this reason, laboratories all over the world are currently testing the magnetic properties of these types of materials. In this connection, the very surface sensitive measurements performed at U5UA on a thin-film surface prepared *in-situ* represent the first measurements available of this kind and do show a largely distinct magnetic behavior on the surface of these materials as compared to their known bulk properties^[4]. ■

[1] D.I. Khomskii, G.A. Sawatzky, *Solid State Comm.* **102**, 87 (1997).

[2] C. Zener, *Phys. Rev.* **81**, 440 (1951).

[3] J.-H. Park, E. Vescovo, H.-J. Kim, C. Kwon, R. Ramesh, and T. Venkatesan, "Observation of a Half-Metallic Ferromagnet", *Nature* (in press, 1997).

[4] J.-H. Park, E. Vescovo, H.-J. Kim, C. Kwon, R. Ramesh, and T. Venkatesan, "Novel Magnetic Properties at Surface Boundary of a Half-Metallic Ferromagnet Manganese Perovskite", submitted to *Science*.

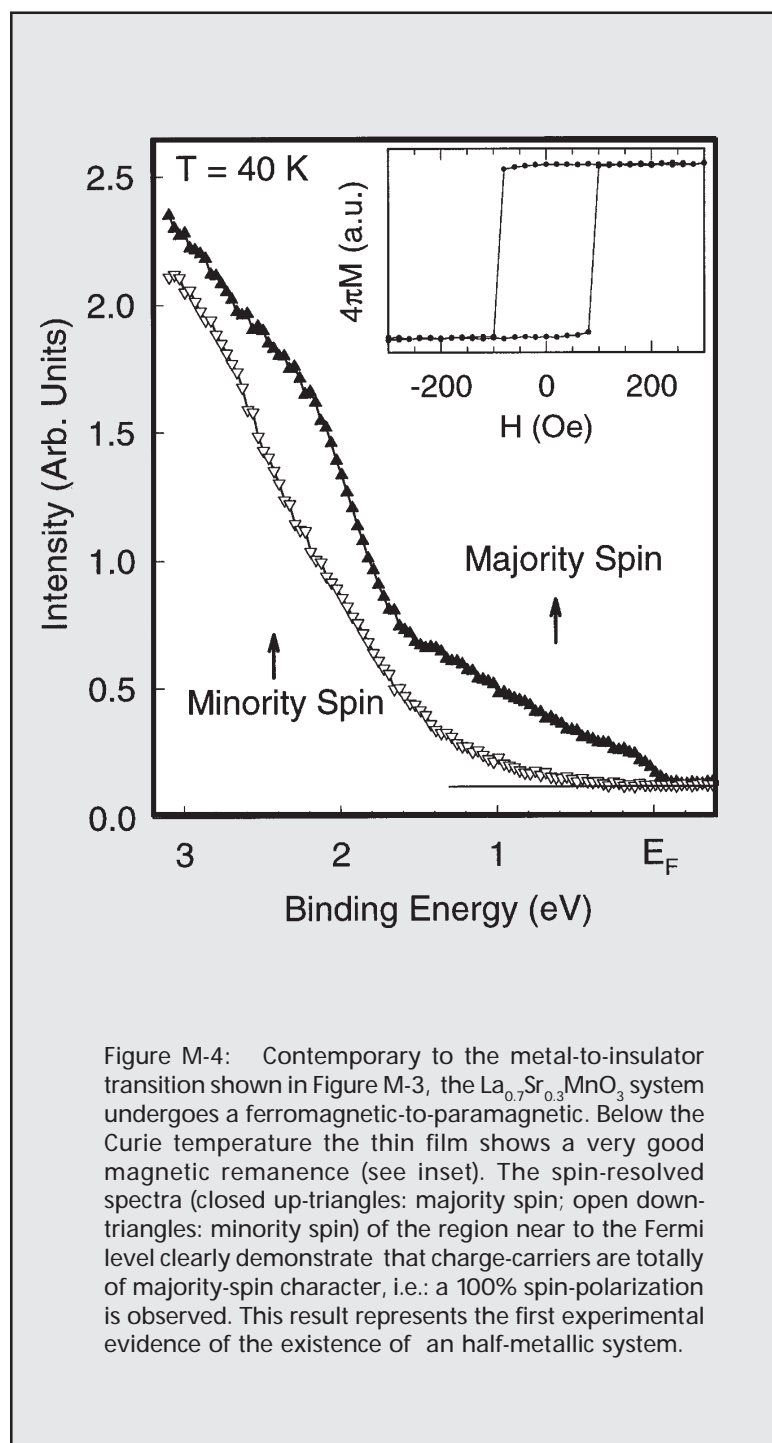


Figure M-4: Contemporary to the metal-to-insulator transition shown in Figure M-3, the $\text{La}_{0.7}\text{Sr}_{0.3}\text{MnO}_3$ system undergoes a ferromagnetic-to-paramagnetic. Below the Curie temperature the thin film shows a very good magnetic remanence (see inset). The spin-resolved spectra (closed up-triangles: majority spin; open down-triangles: minority spin) of the region near to the Fermi level clearly demonstrate that charge-carriers are totally of majority-spin character, i.e.: a 100% spin-polarization is observed. This result represents the first experimental evidence of the existence of an half-metallic system.

The c-axis Optical Response of $\text{Y}_{1-x}\text{Ca}_x\text{Ba}_2\text{Cu}_3\text{O}_{7-\delta}$ Single Crystals Studied by Far Infrared Ellipsometry

C. Bernhard, R. Henn, A. Wittlin, W. König, and M. Cardona
(Max-Planck-Institut für Festkörperforschung)

The incoherent electronic c-axis conductivity $\sigma_c^{\text{el}}(\omega, T)$ of the cuprate high- T_c superconductors has attracted considerable attention. The most peculiar feature is the gap-like suppression of the normal state $\sigma_{1c}^{\text{el}}(\omega, T)$ in the far infrared (FIR) regime which has recently been observed in underdoped $\text{YBa}_2\text{Cu}_3\text{O}_{7-\delta}$ (Y-123)^[1,2], $\text{YBa}_2\text{Cu}_4\text{O}_8$ ^[3] and possibly also in $\text{La}_{2-x}\text{Sr}_x\text{CuO}_4$ ^[4,5]. This observation has raised the question of whether the unusual properties of the FIR c-axis conductivity are related to the pseudogap which depletes the low energy spin- and charge excitations of the CuO_2 planes^[6] rather than to the insulating rocksalt layers which separate the metallic CuO_2 planes acting like “blocking layers”^[7]. In the former case $\sigma_{1c}^{\text{el}}(\omega, T)$ should evolve as a function of the hole doping of the CuO_2 planes, in analogy to the pseudogap which occurs only for underdoped samples and disappears around optimum doping^[6]. In the latter case the anomalous features of $\sigma_{1c}^{\text{el}}(\omega, T)$ should depend critically on the structural and electronic details of the “blocking layers”^[7]. In particular, for Y-123 the CuO chains should have a pronounced influence since they become metallic upon oxygenation and reduce the effectiveness of the “blocking layer”.

In order to resolve this question we have performed ellipsometric measurements of the FIR c-axis conductivity on $\text{Y}_{1-x}\text{Ca}_x\text{Ba}_2\text{Cu}_3\text{O}_{7-\delta}$ (Y,Ca-123) single crystals for $x=0$ and $x=0.14$ and variable oxygen deficiency δ ^[8]. The partial substitution of Y^{3+} by Ca^{2+} introduces extra hole carriers into the CuO_2 planes in addition to those that are transferred from the CuO chains as controlled by the oxygen content^[9]. This enables us to access almost the entire doping range from underdoped to strongly overdoped. Furthermore, the opposing effects of hole doping due to Ca-substitution and hole depletion due to a deoxygenation of the CuO chains allows us to study samples with a comparable doping state of the CuO_2 planes but a significantly different oxygen content and thus electronic properties of the CuO chains.

The ellipsometry measurements have been performed at the U4IR beamline of the National Synchrotron Light Source (NSLS) at Brookhaven National Laboratory (BNL), using a home-built setup attached to a Nicolet Fourier Spectrometer^[5,10]. The high brilliance of the synchrotron allows us to perform accurate

measurements on crystals with ac-faces as small as $1 \times 0.3 \text{ mm}^2$. The ellipsometry technique provides significant advantages over conventional reflection methods. Ellipsometry is self normalizing and does not require a reference sample. The real- and the imaginary part of the dielectric function are obtained directly without a Kramers-Kronig transformation.

Figure M-5 shows $\sigma_{1c}^{\text{el}}(\omega, T)$ for $\text{Y}_{0.86}\text{Ca}_{0.14}\text{Ba}_2\text{Cu}_3\text{O}_{7-\delta}$ in order of increasing oxygen content and doping. **Figure M-6** shows the data for Ca-free Y-123 which is more fully oxygenated at a given doping state. The oxygen deficiency of the crystals can be estimated from the spectral weight of the phonon mode at 620 cm^{-1} which increases with the oxygen deficiency of the crystal since it involves the vibration of an apex oxygen next to an empty chain fragment^[1,2]. There are five more IR-active modes superimposed on the electronic background which will not be further discussed here.

From **Figures M-5 and M-6** it is evident that a gap-like suppression of $\sigma_{1c}^{\text{el}}(\omega, T)$ in the normal state occurs only for the underdoped samples. The normal state gap in $\sigma_{1c}^{\text{el}}(\omega, T)$ disappears around optimum doping. In the overdoped regime $\sigma_{1c}^{\text{el}}(\omega, T)$ exhibits a metallic T- and ω -dependence. The oxygen content of the CuO chains and the related electronic properties of the “blocking layers” do not affect the characteristic T- and ω -dependence but merely affect the absolute values of $\sigma_{1c}^{\text{el}}(\omega, T)$. This finding implies that pseudogap correlations which deplete the low energy spin- and charge excitations of the CuO_2 planes^[6] may cause the gap-like suppression of $\sigma_{1c}^{\text{el}}(\omega, T)$ and the confinement of the charge carriers in the normal state.

In the overdoped regime this confinement is gradually relaxed while the SC state deteriorates. Both T_c and the SC energy gap 2Δ (as estimated from the onset of the loss of spectral weight in the SC state when the carriers condense into a delta function at zero frequency) are suppressed. In addition a growing fraction of the quasi-particles remains unpaired in the SC state possibly due to strong pair-breaking effects^[8,11]. This raises the question whether the pseudogap and the confinement are necessary prerequisites for the occurrence of high- T_c superconductivity in the cuprates. ■

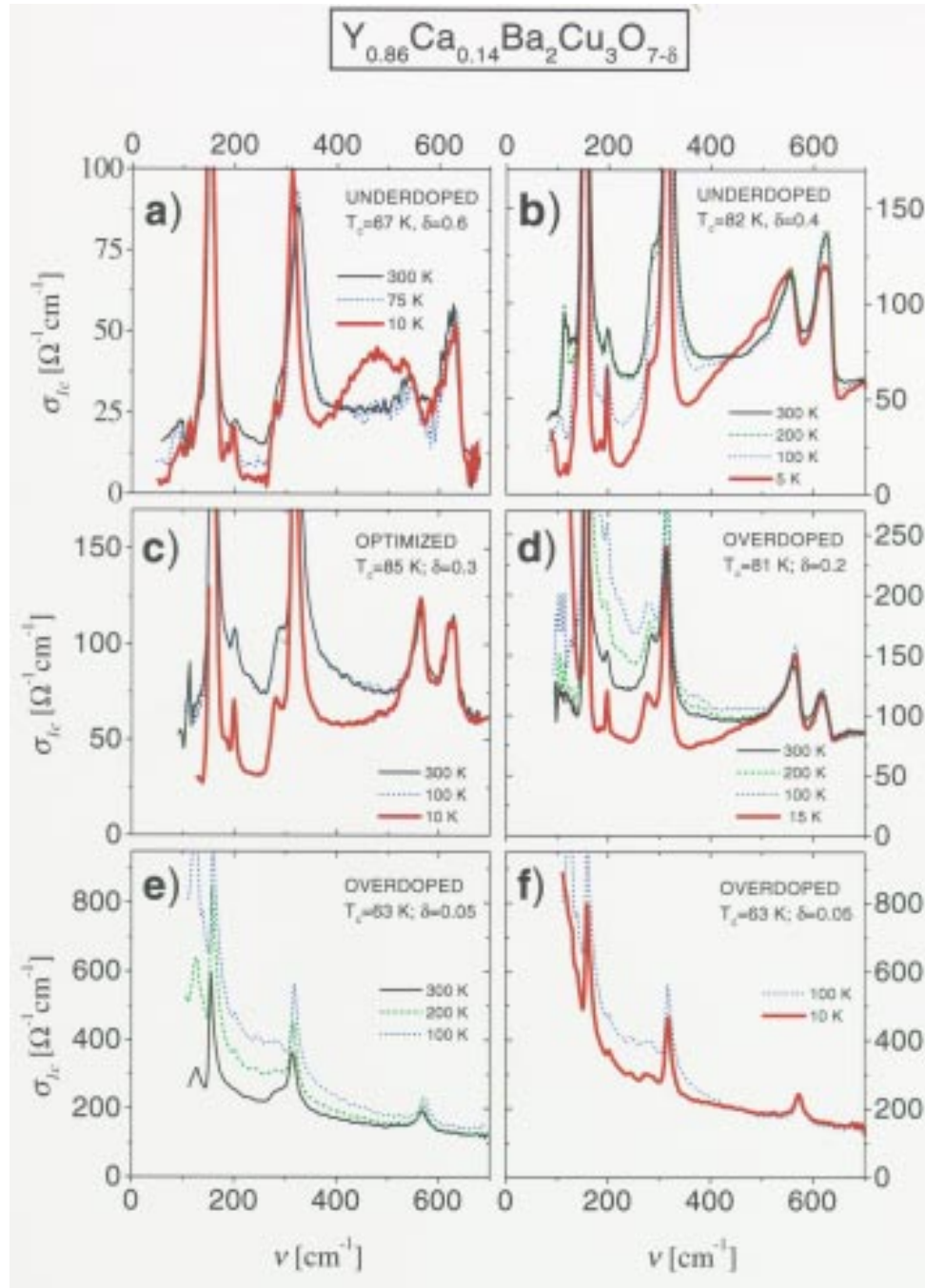


Figure M-5: The real part of the FIR c-axis conductivity $\sigma_{lc}(\omega, T)$ of the $\text{Y}_{0.86}\text{Ca}_{0.14}\text{Ba}_2\text{Cu}_3\text{O}_{7-\delta}$ single crystals with variable oxygen deficiency δ and doping of a) $\delta=0.6$, $T_c=67$ K (underdoped); b) $\delta=0.35$, $T_c=82$ K (underdoped); c) $\delta=0.3$, $T_c=T_{c,\text{max}}=85$ K (optimally doped); d) $\delta=0.2$, $T_c=81$ K (overdoped); and e, f) $\delta=0.05$, $T_c=63$ K (overdoped). The data are shown in the SC state by the red solid lines, in the normal state just above T_c by the blue dotted lines, at intermediate temperatures by the green dashed lines and at room temperature by the black solid lines.

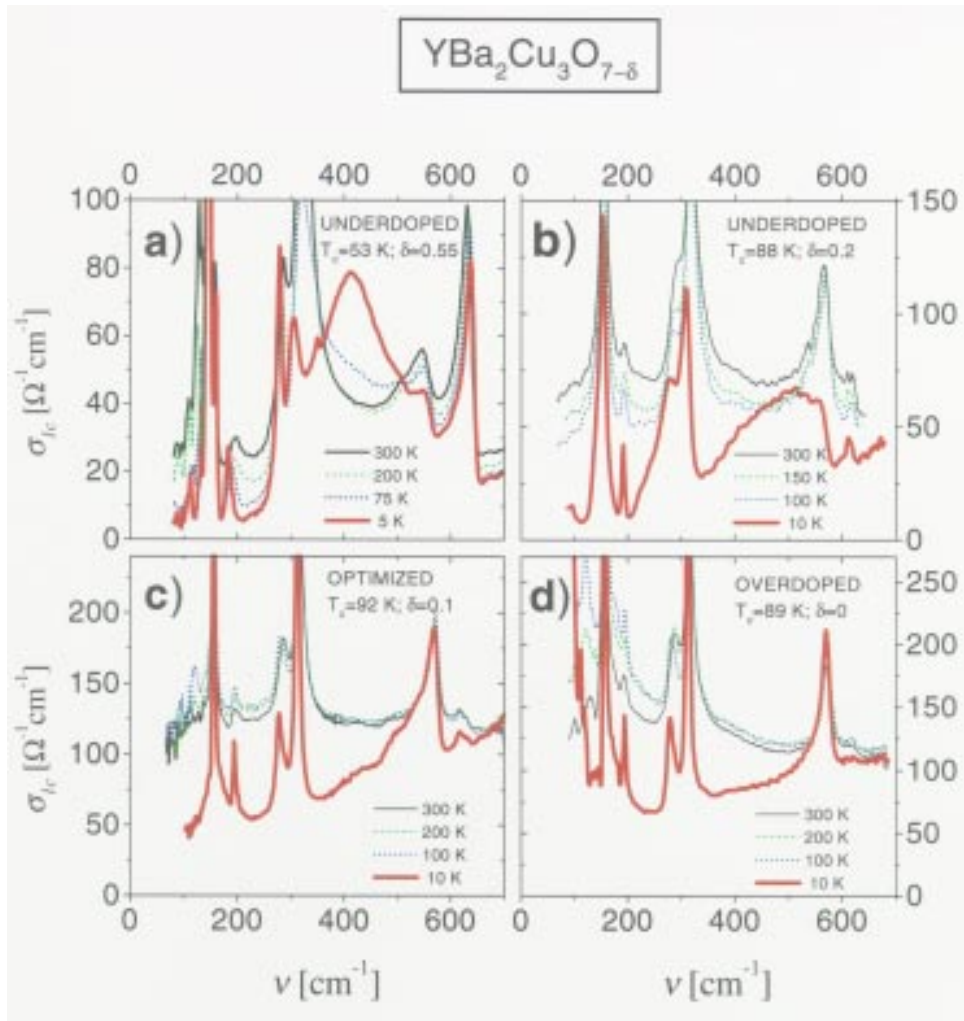


Figure M-6: The real part of the FIR c-axis conductivity $\sigma_{1c}(\omega, T)$ of $\text{YBa}_2\text{Cu}_3\text{O}_{7-\delta}$ single crystals for variable oxygen deficiency and doping of **a)** $\delta \approx 0.55$, $T_c = 53$ K (underdoped); **b)** $\delta \approx 0.2$, $T_c = 88$ K (underdoped); **c)** $\delta \approx 0.1$, $T_c = T_{c, \text{max}} = 92$ K (optimally doped); and **d)** $\delta \approx 0$, $T_c = 89$ K (overdoped). The data are shown in the SC state by the red solid lines, in the normal state just above T_c by the blue dotted lines, at intermediate temperatures by the green dashed lines and at room temperature by the black solid lines.

Acknowledgements. We are indebted to G.P. Williams and L. Carr for support at the U4IR beamline of the NSLS and acknowledge D. Böhme for technical help. We thank M. Kläser, T. Wolf and C.T. Lin for providing the crystals.

- [1] C.C. Homes *et al.*, *Phys. Rev. Lett.* **71**, 1645 (1993).
- [2] J. Schützmann *et al.*, *Phys. Rev.* **B52**, 13665 (1995).
- [3] D.N. Basov *et al.*, *Phys. Rev. B* **50**, 3511 (1994).
- [4] K. Tamasaku *et al.*, *Phys. Rev. Lett.* **72**, 3088 (1994).
- [5] R. Henn *et al.*, to be published in *Thin Solid Films*, R. Henn *et al.*, *Phys. Rev. B* **56**, 6295 (1997).
- [6] J.W. Loram *et al.*, *Phys. Rev. Lett.* **71**, 1740 (1993); A.G. Loesser *et al.*, *Science* **273**, 325 (1996); G.V.M. Williams *et al.*, *Phys. Rev. Lett.* **78**, 721 (1997).
- [7] A.A. Abrikosov, *Phys. Rev. B* **52**, 7026 (1995); *Physica C* **258**, 53 (1996); W.A. Atkinson and J.P. Carbotte, *Phys. Rev. B* **55**, 3230 (1997).
- [8] C. Bernhard *et al.*, to be published in *Phys. Rev. Lett.*
- [9] J.L. Tallon *et al.*, *Phys. Rev.* **B51**, 12911 (1995).
- [10] J. Kircher *et al.*, *J. Opt. Soc. Am.* **B14**, 705 (1997).
- [11] C. Bernhard *et al.*, *Phys. Rev. Lett.* **77**, 2304 (1996).

Surface Alloys: An Auger Photoelectron Coincidence Spectroscopy Study

R.A. Bartynski, and Q. Qian (Rutgers University), and S.L. Hulbert (NSLS)

The VUV Ring has seen considerable utilization by a number of novel applications including Auger-photoelectron coincidence spectroscopy (APECS). In this adaptation of photoelectron spectroscopy both the core photoelectron and the Auger electron associated with a given photoexcitation/decay event are detected in time coincidence. Examining the photoemission spectrum with this additional level of discrimination results in higher surface sensitivity and enables site-specific electronic structure studies while eliminating secondary electron background and lifetime broadening.

Perhaps most exciting results are in the field of surface alloys. We have successfully made the first direct measurement of valence band energy shifts in a surface alloy: Ag/Cu(100). In recent years, there has been considerable theoretical and experimental interest in surface alloys (bimetallic systems that intermix only in the first atomic layer) owing to their novel electronic, chemical, and magnetic properties. First principles electronic structure calculations suggest that band narrowing and a systematic shift (as a function of host) in the valence levels of the minority species lead to the

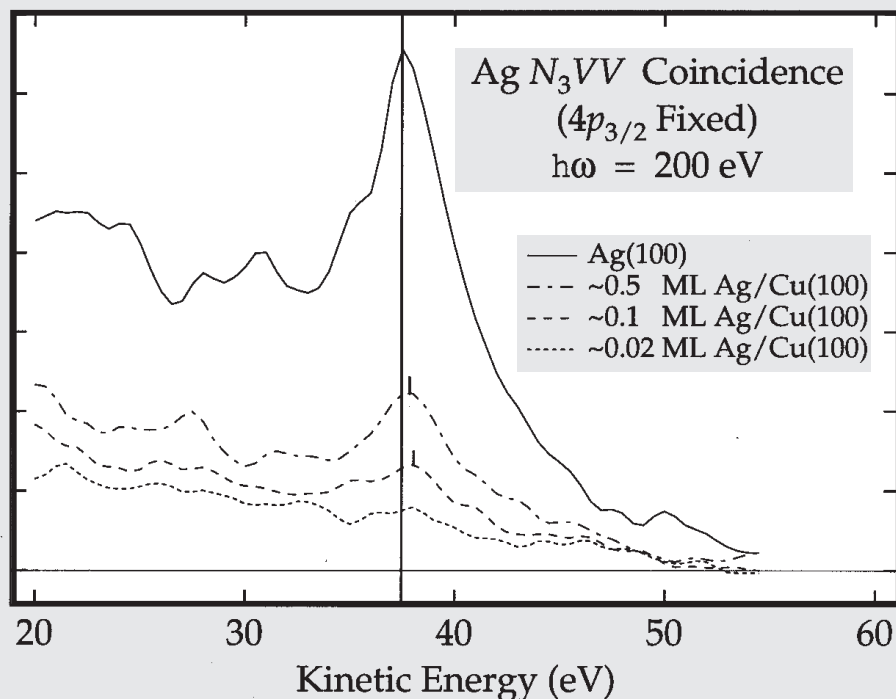


Figure M-7: Auger photoelectron coincidence spectroscopy (APECS) Ag N_3VV Auger spectra from Ag(100) and from the Ag/Cu(100) system for three Ag coverages as indicated. These spectra were taken in time coincidence with Ag $4p_{3/2}$ photoelectrons excited with 200eV photons.

unusual physical properties of these systems. Up until now, experimental work has focused on structural aspects, particularly STM measurements exploring phase formation upon intermixing at the surface. Measurements of the electronic structure using conventional photoelectron spectroscopy are extremely difficult because the signal from the minority metal typically is weak and often overlaps spectral features of the substrate.

Our primary result is summarized in **Figure M-7**. Here, APECS spectra of the $\text{Ag N}_{2,3}\text{VV}$ Auger transition from $\text{Ag}(100)$ are compared to that of the $\text{Ag}/\text{Cu}(100)$ system for several Ag coverages. As is clear from the figure, the peak in the coincidence Auger spectrum shifts to higher kinetic energy for low Ag concentrations. This shows that the Ag d -levels shift closer to the Fermi level as compared to Ag metal. STM studies indicate that for coverages in the 0.1 monolayer (ML) range, Ag forms a random substitutional alloy in the $\text{Cu}(100)$ surface. The calculations predict that in this phase, the centroid of the Ag d -band shifts ~ 0.70 eV away from the Fermi level.

The origin of the difference between our experimental results and the theory is not yet clear, however the shifts can be understood in terms of relative electron density and the calculations were performed for the closed packed surface, while our experiments examined the more open (100) surface. Upcoming investigations of $\text{Pt}/\text{Cu}(100)$ and $\text{Pt}/\text{Ag}(100)$ should prove most interesting.

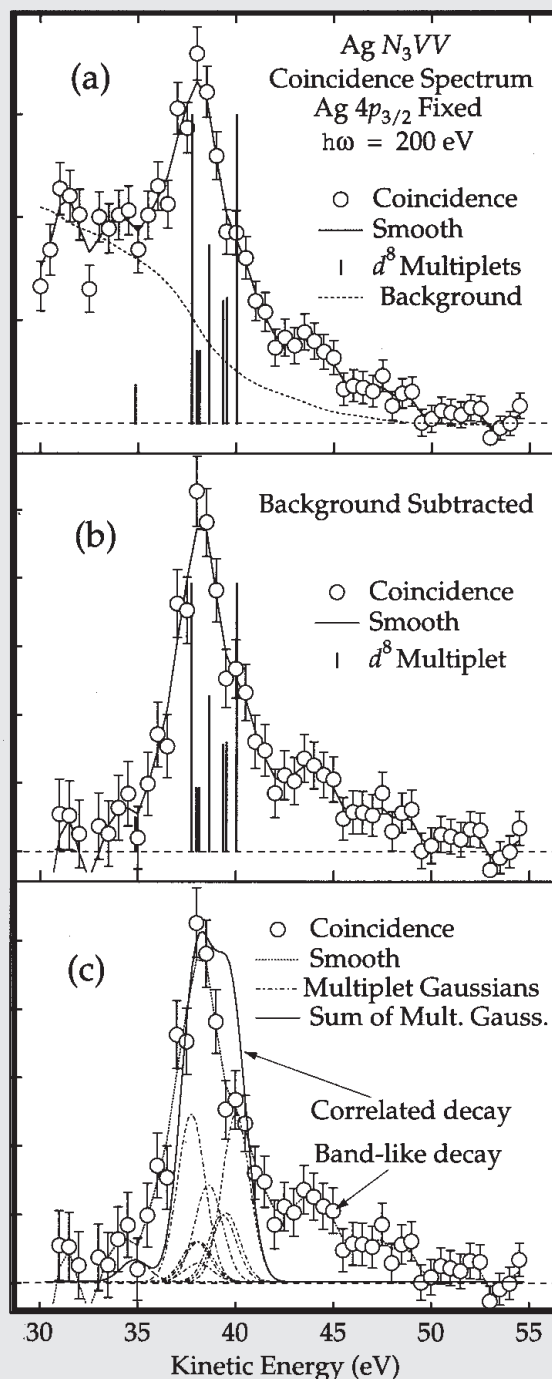


Figure M-8: (a) $\text{Ag N}_{2,3}\text{VV}$ coincidence Auger spectrum (circles) of the $\text{Ag}(100)$ surface taken in time coincidence with $\text{Ag } 4p_{3/2}$ photoelectrons excited with 200eV photons. Digital smooth (solid line), multi-electron background (dotted line) and atomic-like d^8 multiplets (vertical solid bars) are shown. (b) Background-subtracted (from (a)) $\text{Ag N}_{2,3}\text{VV}$ coincidence Auger spectrum of the $\text{Ag}(100)$ surface. (c) same as (b) except d^8 multiplets are Gaussian-broadened. The sum of the broadened multiplets is shown (solid line, labeled "Correlated decay").

To better understand the influence of alloying on the electronic structure of the minority component, we have also performed detailed studies of the Ag 4p core levels and the associated $N_{2,3}VV$ Auger spectra from the single crystal Ag(100) surface. It is well known that the shallow p-levels of the late transition metals have very broad and ill-defined spectral line shapes. Owing to strong overlap with the 4d bands, the shallow 4p levels of Ag have a very short lifetime and hence appear as broad (~5 eV wide) features in photoemission spectra. This width is folded into the conventional Auger spectrum. By measuring Ag $N_{2,3}VV$ Auger electrons in coincidence with Ag 4p photoelectrons of a particular kinetic energy, we have eliminated this broadening and revealed the intrinsic lineshape of the Auger transition. These coincidence Ag N_3VV Auger spectra are shown in **Figure M-8**. The majority of the emission is accounted for by an atomic-like d^8 multiplet, but there is a significant band-like component. A comparison of the relative spectral weight contained in each component indicates that the band-like part is larger than is observed in conventional $M_{4,5}VV$ Auger spectra and also larger than is anticipated based on the band width and correlation energies of Ag. ■

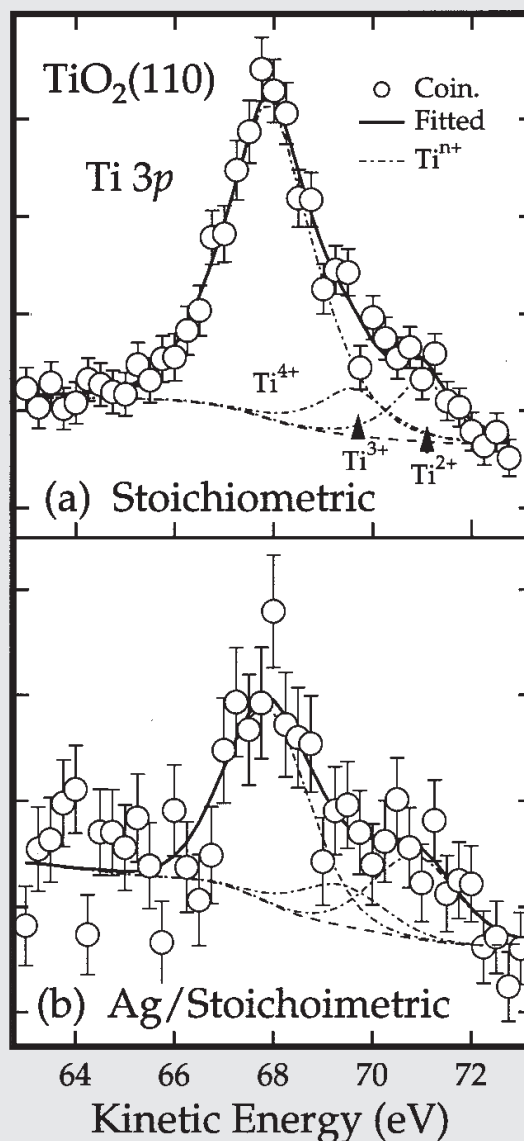


Figure M-9: (a) Ti 3p core level spectrum from the clean, stoichiometric $TiO_2(110)$ surface taken in time coincidence with Ti MVV Auger electrons. The Ti^{4+} main peak, and shoulders assigned to Ti^{3+} and Ti^{2+} oxidation states, associated primarily with surface oxygen vacancies and step edges, respectively, are labeled. (b) same as (a), but acquired after ~ 0.2 monolayer (ML) of Ag is adsorbed on the surface.

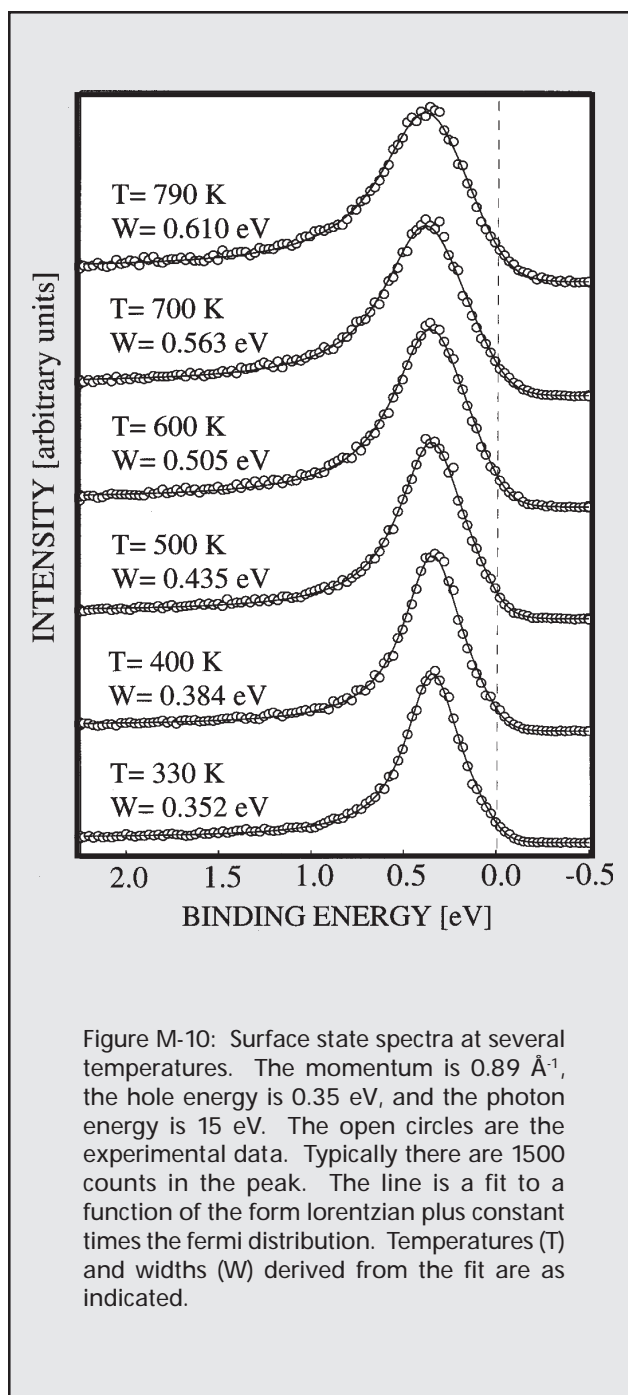
Large Value of the Electron-Phonon Coupling Parameter $\lambda=1.15$ and the Possibility of Surface Superconductivity at the Be(0001) Surface

T. Balasubramanian and E. Jensen (Brandeis University)
X.L. Wu and S.L. Hulbert (NSLS)

The electronic density of states (DOS) at the Fermi level (E_F) at the Be(0001) surface is about four times larger than in the bulk^[1]. The E_F DOS is an important parameter for describing many electronic processes. Anomalously large surface core level shifts^[2], and giant surface Friedel oscillations^[3] have been observed on this surface, and attributed to the large surface to bulk E_F DOS ratio. Electron phonon coupling should also be enhanced. In a typical electron-phonon interaction event, an electron scatters from one state to another with the emission or absorption of a phonon. By simple Fermi golden rule arguments, one expects the probability for this interaction to be proportional to the density of states into which the electron can scatter. Phonon and thermal energies are small on the scale of electronic energies and the final state energy is near to E_F , so the coupling is proportional to the electronic density of states at E_F . The strength of the electron-phonon interaction is conventionally measured by the dimensionless parameter λ , called the mass enhancement or coupling parameter. Accordingly, one should expect λ_s at the Be(0001) surface to be near unity, four times larger than the bulk value $\lambda_b=0.24$.

It has been shown that angle resolved photoemission (ARP) can be used to determine λ_s for crystalline metal surfaces^[4]. The basic idea is that, under proper conditions, the observed width of a surface state peak is equal to \hbar/τ , where τ is the lifetime of the surface state hole excitation. Since virtually all of the temperature dependence of τ is in the phonon contribution, a measurement of the temperature dependence of the surface state width is effectively a measurement of the temperature dependence of the phonon contribution to the hole lifetime. At high temperatures and small hole energies the temperature dependence of the phonon contribution to the inverse hole lifetime is given by $\hbar/\tau = 2\pi kT$. In this limit, λ is just $2\pi k$ times the slope of the peak width vs. temperature curve, and is easily measured.

We have used ARP to determine λ_s at the Be(0001) surface and find that $\lambda_s=1.15$, more than four times larger



than λ_b . The data and analysis are presented in the figure below.

It is common for large values of λ to be associated with high superconducting T_c 's, especially in materials such as Be with large phonon energies. If the surface is considered as a thin film with high λ on a thick substrate with low λ , the proximity effect would destroy any observable interesting effects. However, it was shown by Suhl, Matthias, and Walker^[5] that different branches of the Fermi surface — for which surface and bulk states qualify — could have different superconducting energy gaps. In the limit of a semi-infinite solid the two branches are essentially uncoupled and the surface states are allowed to superconduct independent of the bulk. Application of the McMillan formula using bulk phonons to estimate the superconducting transition temperature yields 70K for the surface transition temperature.

Impurities/defects will likely play a more important role in destabilizing this system than they do in homogeneous superconductors. The problem is that the impurities scatter surface states into bulk states, the one electron eigenstates become linear combinations of surface and bulk states, and the pairing interaction is averaged over surface and bulk. Since the interaction in the bulk is weak, any averaging will quickly destroy superconductivity at the surface. It is known that two band effects are destroyed if the mean free path is shorter than the superconducting coherence length^[6]. For the Be(0001) surface, assuming a 70K T_c , ξ_0 is about 300Å. A mean free path as large as this is difficult to achieve on a metal surface. However, only the interband (surface to bulk) scattering should contribute to the averaging. Since the surface state DOS is much larger than the bulk state DOS, surface to surface scattering should be much more common than surface to bulk scattering, and a much smaller mean free path may be adequate.

If the surface states do pair at elevated temperatures, they represent an interesting opportunity to study two dimensional superconductivity for a simple system with a relatively large energy scale. The one electron origins of the many body state are simple and well characterized (parabolic bands, nearly circular Fermi surface), and the pairing mechanism (phonons) is well understood. The superconducting gap energy ought to be resolvable by high resolution ARP spectrometers. Scanning tunneling microscopy should also be able to observe the gap. Simple estimates of the maximum surface current density are of order 10 Å/cm, so the change in resistivity at T_c may be directly observable as well. ■

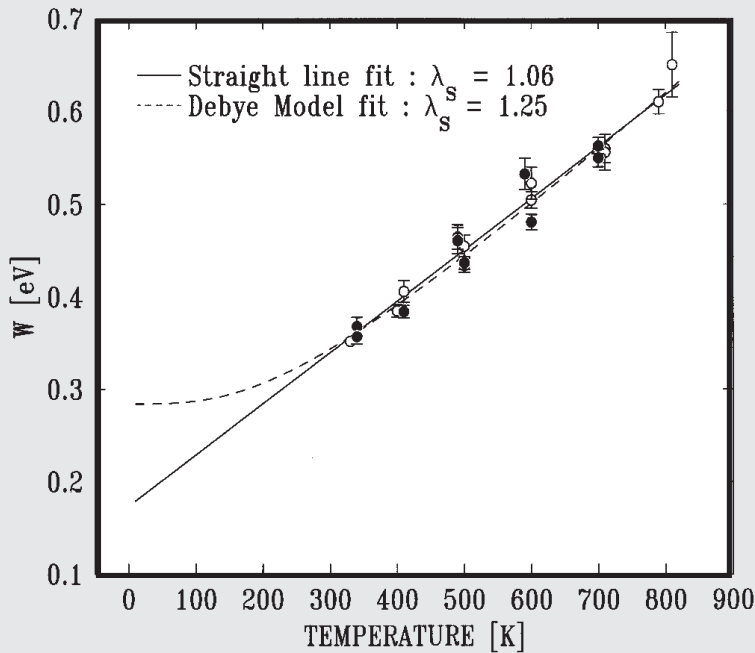


Figure M-11: Surface state widths from fits like those shown in Figure M-10 vs. temperature. These data include two full cycles from room temperature to 800K and back to room temperature. The error bars on the data are statistical uncertainties from the fits. The open circles are for increasing temperature and the filled circles are for decreasing temperature. This analysis assumes that all of the temperature dependence of the widths comes from phonon creation/annihilation. In the limit of high temperatures, not quite realized for these data, λ is proportional to the derivative of the width with respect to temperature^[4]; a more accurate analysis results from a fit to the Debye model.

- [1] E.V. Chulkov *et al.*, *Surf. Sci.* **188**, 287, (1987).
- [2] L.I. Johansson *et al.*, *Phys. Rev. Lett.* **71**, 2453, (1993).
- [3] P.T. Sprunger *et al.*, *Science* **275**, 1764, (1997).
- [4] McDougall, Balasubramanian, and Jensen, *Phys. Rev. B* **51**, 13891, (1995).
- [5] Suhl, Matthias, and Walker, *Phys. Rev. Lett.* **3**, 552, (1959).
- [6] B.T. Gelikman *et al.*, *Sov. Phys. Sol. St.* **9**, 642, (1967).

Characterizing Interfacial Magnetic Roughness

J. Freeland and Y. Idzerda (NRL)

Industrial production of magnetic devices and media (computer hard disks, read/write heads, magnetic memory, etc.) is undergoing an explosion in size similar to that experienced by the semiconductor industry a decade ago. However, many effects that are not well understood plague the behavior of these systems. One of essential importance is the disorder of magnetic moments at the interface (i.e. magnetic roughness). Since these magnetic devices consist of thin layers ($\sim 10^{-7}$ cm) of ferromagnetic (FM) and non-magnetic (NM) materials, roughness at the boundary between the FM and NM materials can dramatically alter the magnetic behavior. Recently our group (John Freeland, Varoujan Chakarian, Konrad Bussmann, Yves Idzerda, and Chi-Chang Kao) at the NRL/NSLS Magnetic Circular Dichroism Facility (located at beamline U4B of the NSLS) has been studying the interdependence of magnetic and chemical interfaces.

We find that the magnetic and chemical roughnesses of a NM/FM interface are distinctly different. This

means that to obtain a full picture of how roughness influences the magnetic properties, one must obtain information concerning both the magnetic and chemical interfaces. The formalism for the determination of the nature of chemical interfaces and surfaces using specular and off specular (diffuse) scattering is a well established field, but only recently has it become possible to directly probe the magnetic interface. To probe information about a magnetic interface one needs a significant magnetic scattering signal. One way of providing this is through the resonant enhancement of the magnetic and chemical scattering when an incident circular polarized photon is tuned to an absorption edge, known as x-ray resonant magnetic scattering (XRMS). Utilization of a circular polarized photon, like its absorption counterpart Magnetic Circular Dichroism (MCD), generates the magnetic scattering component. By measuring sample rocking curves at the L_3 absorption edge, we can extract information concerning not only the chemical but also the magnetic interface.

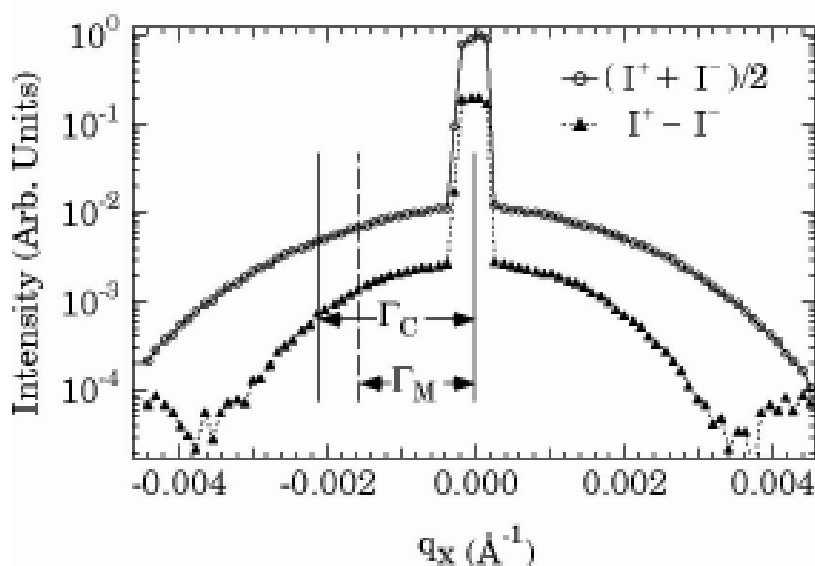


Figure M-12: Sample rocking curve measured at the Co L_3 (778 eV) for chemical and magnetic contributions vs. q_x . This scan was taken at a detector angle 2θ of 90. Notice how the half width of the magnetic diffuse (GM) is smaller than that of the chemical diffuse (GC) indicating a longer correlation length, χ , for the magnetic interface.

To explore how an NM/FM interface varies with roughness we utilized a series of CoFe thin films where an increasing chemical roughness was induced through the growth process. **Figure M-12** shows the chemical and the magnetic contributions to a sample rocking (diffuse) scan measured at the Co L_3 edge. From the analysis of these rocking curves we find a distinctly different behavior of both perpendicular (s) and in-plane (x) roughness for the chemical vs. magnetic interfaces. To test the interdependence of the chemical and magnetic roughness we have measured a series of samples with varying chemical roughness, as determined by Atomic Force Microscopy (AFM), where the roughness variation is generated by a thickness variation in Cu growth

template prior to magnetic multilayer deposition. As seen in **Figure M-13**, the magnetic roughness in this series of samples typically ~20-30% less than the chemical roughness. The same is seen for the behavior of the chemical vs. magnetic correlation length (bottom panel of **Figure M-13**). This indicates that the magnetic interface is typically much smoother than the chemical interface both perpendicular and in the plane of the film. These results illustrate clearly that one cannot understand the influence of roughness by only exploring the chemical interface. Not all magnetic properties are affected in the same way by interfacial disorder, so only by having the complete picture can we begin to obtain an understanding.

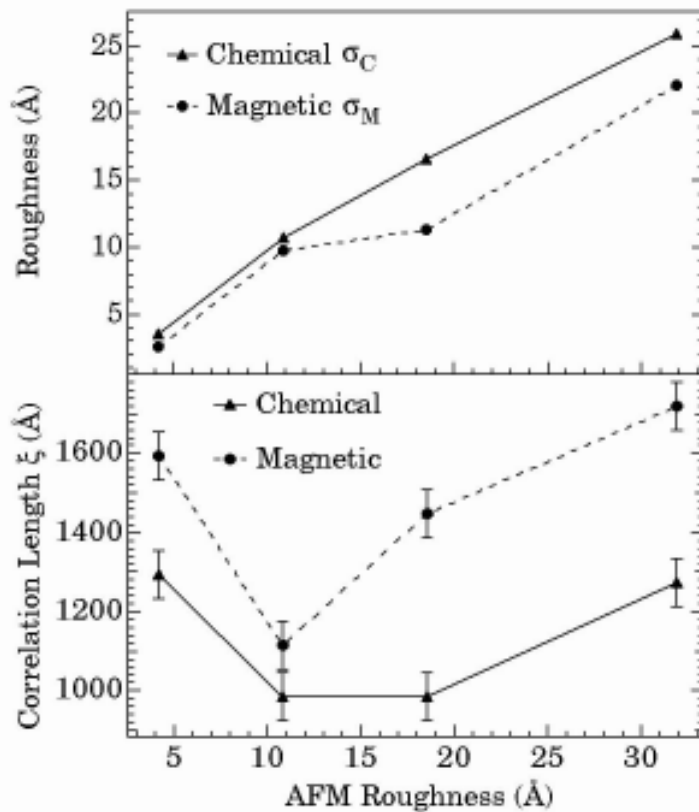


Figure M-13: Perpendicular (s) and in-plane (x) roughness parameters derived from the diffuse scattering data. Top panel: chemical and magnetic rms roughness. Bottom panel: chemical and magnetic correlation lengths.

In addition to our work studying NM/FM interfaces, we are also trying to better our understanding of diffuse XRMS technique. Due the dramatic changes in the scattered intensity near the absorption edge, we undertook a study of the diffuse intensity not only as a function of q_x but also energy of the incident photon. **Figure M-14** shows the results of such a measurement. Notice in particular how by only changing the incident photon by a few eV the shape of the diffuse intensity (both magnetic and chemical) can be altered significantly. While these resonant changes appear very different they contain the same information concerning the interface. Analysis of this data will not only further our understanding of this technique, but will also provide a testing ground for theories of diffuse XRMS.

Our current work has brought our understanding to a point where we stand on the threshold of being able to explore a wide variety of problems related to magnetic heterostructures of extreme interest to many facets of the magnetism community. ■

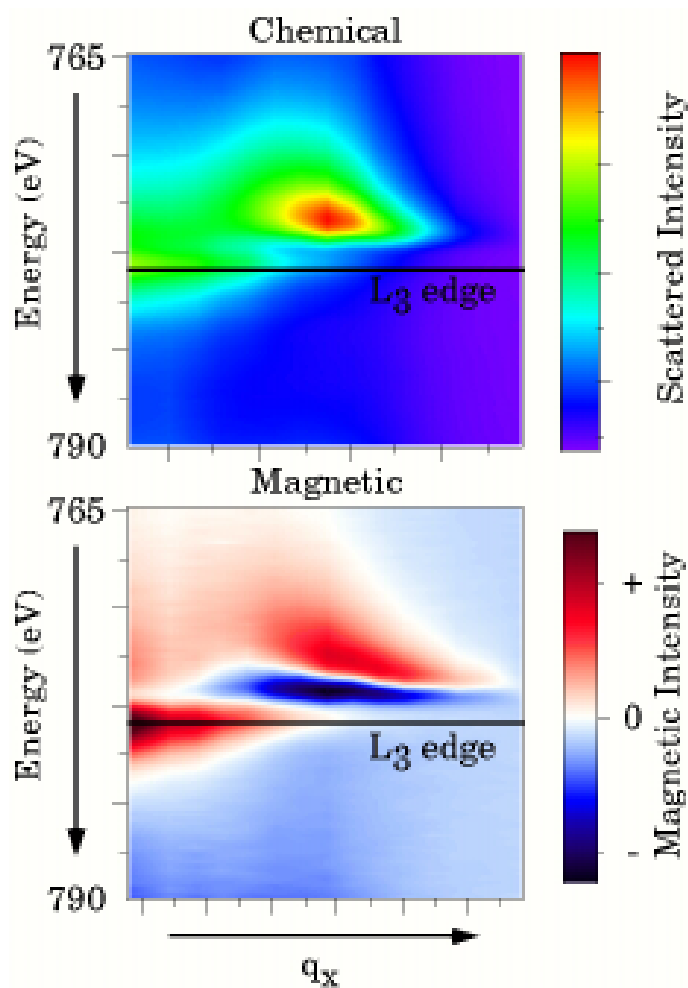


Figure M-14: Diffuse intensity as a function of q_x and incident photon energy. The black line shows the cut along q_x at the Co L₃ edge that yields the data in Figure M-12.

Resonant Inelastic Scattering Studies of 4f rare Earth Compounds

F. Bartolome, J.M. Tonnerre, L. Seve, and D. Raoux (CNRS, France), J. Chaboy and L.M. Garcia (Instituto de Ciencia de Materiales de Aragón, Spain), M. Krisch (ESRF), and C.-C. Kao (NSLS)

A systematic study of the $2p_{3/2}-3d_{5/2}$ or $2p_{3/2}-4d_{5/2}$ resonant inelastic scattering of 4f rare earth compounds ($R = \text{Nd, Sm, Gd, Tb, Dy, Ho, Er, and Tm}$) was carried out by Bartolome *et al.* [1] An E2 ($2p(4f)$) quadrupolar absorption channel was observed for all the compounds studied. Energy separation between the dominant E1 ($2p(5d)$) dipole absorption energy and the weak E2 absorption energy was also measured systematically. A double-peaked preedge feature was observed for light rare earth ions, and was interpreted as two intermediate states

corresponding to the excitations of the two possible spins of the excited photoelectron. Detailed comparison was also made with corresponding x-ray magnetic circular dichroism (XMCD) spectra to show that the origin of the low energy XMCD effect from all rare earth ions is due to E2 absorption channel, and that the sign change in the XMCD signal from light rare earth ions to heavy rare earth ions is due to the double-peaked pre-edge absorption feature in light rare earth ions. ■

Resonant Inelastic Scattering Study of Nd_2CuO_4

J.P. Hill, C.-C. Kao, W.A.C. Caliebe (BNL), M. Mastubara, A Kotani (ISSP, Tokyo), J.L. Peng and R.L. Greene (University of Maryland, College Park)

Resonant inelastic scattering study of Nd_2CuO_4 , the parent compound of the electron doped high temperature superconductor $\text{Nd}_{2-x}\text{Ce}_x\text{CuO}_4$, at the Cu K absorption edge was reported [2]. Resonant enhancement of the charge transfer excitations, similar to the observation in NiO , was observed. An Anderson impurity model which includes both the intra-atomic Coulomb interactions and $\text{Cu}(3d)\text{-O}(2p)$ interatomic hybridization, was used to interpret the data. The model calculations agree well with both the observed energy loss and the excitation energy dependence of the scattering intensity. And the observed energy loss of 6eV

is assigned to excitation from the ground state to the anti-bonding state of the CuO_6 cluster. There is also indication that non-local effects are important in the interpretation of these spectra. ■

[1] F. Bartolome, J.M. Tonnerre, L. Seve, D. Raoux, J. Chaboy, L.M. Garcia, M. Krisch, C.-C. Kao, "Identification of Quadrupolar Excitation Channels at the L III_{II} Edge of Rare Earth Compounds"; *Phys. Rev. Lett.* **79**, 3775 (1997).

[2] Hill *et al.*, submitted *Phys. Rev. Lett.*

Bond-length Distortions in Strained Semiconductor Alloys

J.C. Woicik (NIST)

When a macroscopic body is acted upon by small external forces, its deformations are accurately described by the theory of elasticity^[1]. Despite the maturity of this branch of theoretical physics, the microscopic distortions - bond length and bond angle - which govern the macroscopic behavior of the body are, in general, not well understood, particularly from an experimental point of view. Because the macroscopic-strain state of semiconductor layers can be accurately determined by bulk-sensitive techniques such as x-ray diffraction, strained-layer semiconductors offer a unique vehicle with which to study these microscopic distortions quantitatively.

In order to address the issue of bond-length strain, we^[2] have performed high-resolution extended x-ray absorption fine structure (EXAFS) measurements at the In-K absorption edge (27,940 eV) on a well characterized, buried, 213 Å $\text{Ga}_{0.78}\text{In}_{0.22}\text{As}$ layer grown coherently on GaAs(001). **Figure M-15** shows the EXAFS from the strained layer. These data were recorded at beamline X18B using a Si(111) channel-cut monochromator and a 13 element Ge solid-state detector set to monitor the In- K_{α} fluorescence yield. Also shown is the EXAFS from bulk InAs, recorded in transmission. Both are plotted with their Fourier-filtered first-shell contributions, which correspond to the In-As bond lengths.

To obtain quantitative information, the data from the layer were fit by the function $k\chi(k)$ using the phase and amplitude functions derived from the bulk InAs standard. The fit determines $r'_{\text{InAs}} = 2.581 \pm 0.004$ Å. Because the bond length in bulk InAs is 2.623 Å, the In-As bond length in the strained layer is found contracted 0.042 ± 0.004 Å relative to the In-As bond length in bulk InAs.

In their pioneering study, Mikkelsen and Boyce^[3] used EXAFS to measure the bond lengths in bulk $\text{Ga}_{1-x}\text{In}_x\text{As}$ alloys. They found that, instead of following the virtual-crystal approximation (VCA),

$$r_{\text{VCA}} = (1 - x) r_{\text{GaAs}}^0 + (x) r_{\text{InAs}}^0, \quad (1)$$

the In-As and Ga-As bond lengths maintain two chemically distinct values. Although these distinct values do vary linearly with alloy composition, this variation is only about a quarter (~ 0.04 Å) of the natural bond-length difference between bulk InAs ($r_{\text{InAs}}^0 = 2.623$ Å) and bulk GaAs ($r_{\text{GaAs}}^0 = 2.448$ Å). Using the accurate data of Mikkelsen and Boyce^[3], the In-As and Ga-As bond lengths in a bulk (cubic) $\text{Ga}_{1-x}\text{In}_x\text{As}$ alloy with In content 22% are $r_{\text{InAs}} = 2.596$ Å, and $r_{\text{GaAs}} = 2.455$ Å, respectively. The In-As bond length measured in the strained layer, $r'_{\text{InAs}} = 2.581 \pm 0.004$ Å, is significantly shorter than this value. In fact, it is even shorter than the In-As bond length measured by Mikkelsen and Boyce^[3] in the dilute-

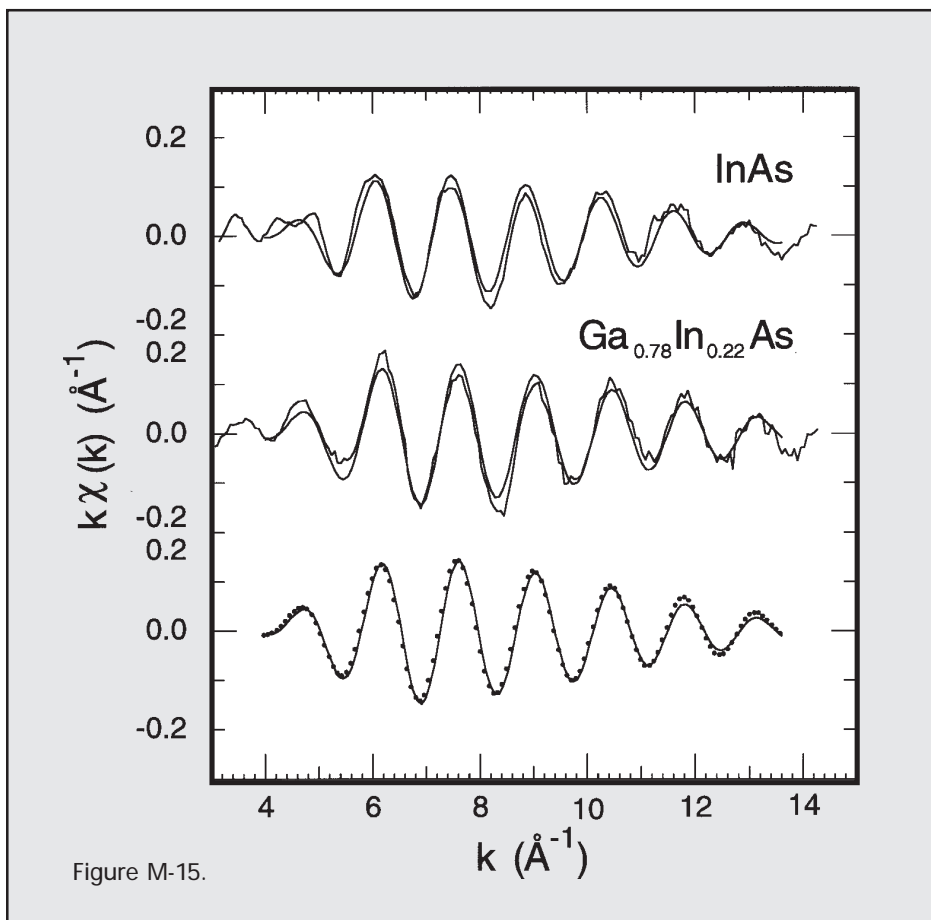


Figure M-15.

alloy limit, $r_{\text{InAs}} = 2.588 \text{ \AA}$ for $x \rightarrow 0$; consequently, it must reflect the external compressive strain imposed on the layer by the substrate: $\Delta r = -0.015 \pm 0.004 \text{ \AA}$.

Because the lattice constant of InAs is 7% larger than the lattice constant of GaAs, pseudomorphic growth of a $\text{Ga}_{1-x}\text{In}_x\text{As}$ alloy on GaAs(001) results in a layer that is compressed bilaterally within the (001) plane of the substrate and Poisson expanded uniaxially along the [001] growth direction. From macroscopic-elastic theory^[4], the fractional strain of the film parallel to the interface, $\epsilon_{//} = (a_{//} - a_f)/a_f$, is related to the fractional strain of the film perpendicular to the interface, $\epsilon_{\perp} = (a_{\perp} - a_f)/a_f$, through the elastic constants c_{11} and c_{12} of the film, its cubic lattice constant a_f , and the coherency condition $a_{//} = a_{\text{GaAs}}$:

$$\epsilon_{\perp} = -2 (c_{12}/c_{11}) \epsilon_{//}. \quad (2)$$

Because the layer is tetragonally distorted, the average virtual-crystal bond length is no longer equal to $\tilde{A}3/4a_f$; however, it may be computed from

$$r' = 1/4 (2 a_{//}^2 + a_{\perp}^2)^{1/2}. \quad (3)$$

Using $a_{//} = a_f + \Delta a_{//}$ and $a_{\perp} = a_f + \Delta a_{\perp}$, it is easily shown that to first order in ϵ

$$r' = \tilde{A}3/4 a_f (1 + 1/3 (2 \epsilon_{//} + \epsilon_{\perp})). \quad (4)$$

Because equation 4 describes the distortion of the *average* bond length in the layer, a further assumption about the *relative* distortions is needed before the bond lengths can be calculated individually. If we assume that the In-As and Ga-As bond lengths change by the same amount despite their inequivalent bond lengths, Eq. 4 together with macroscopic-elastic theory (Eq. 1) renders $r'_{\text{InAs}} = 2.582 \text{ \AA}$, and $r'_{\text{GaAs}} = 2.442 \text{ \AA}$. This value is indistinguishable from our experimental result: $r'_{\text{InAs}} = 2.581 \pm 0.004 \text{ \AA}$.

In order to test the validity of this conclusion, we^[5] have performed a random-cluster calculation of the bond lengths in tetragonally distorted, pseudobinary $\text{Ga}_{1-x}\text{In}_x\text{As}$

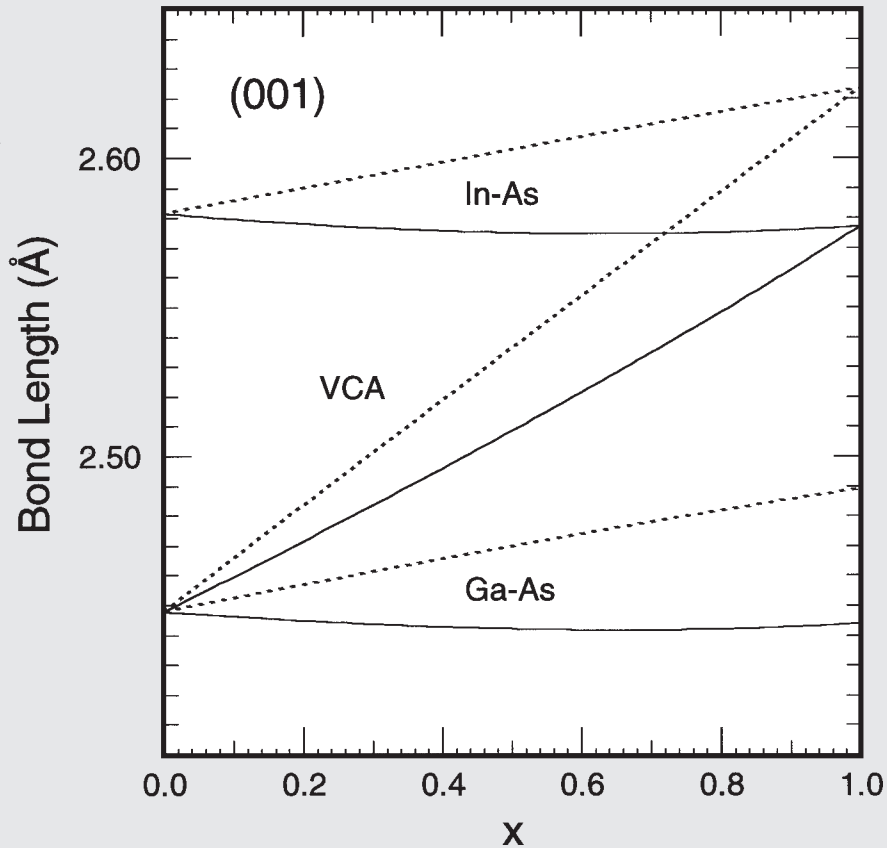


Figure M-16.

alloys on GaAs(001). The calculation was performed by relaxing the atoms within sixteen-bond $\text{Ga}_{4-j}\text{In}_j\text{As}$ clusters ($j = 0, 1, 2, 3, 4$) embedded in virtual-crystal media. The bond lengths were calculated as a function of medium composition x and then statistically averaged. The Keating valence-force field^[6], generalized for the pseudobinary alloy, was used to model the interactions within the clusters:

$$\Delta E = \sum_s \frac{3}{8} \alpha_s (\overline{r_s^2} - r_{s,0}^2)^2 + \sum_{s < t} \sum_t \frac{3}{8} \beta_{s,t} (\overline{r_s \cdot r_t} - r_{s,0} \cdot r_{t,0})^2. \quad (5)$$

The α_s 's are the two-body radial-force constants, and the $\beta_{s,t}$'s are the three-body angular-force constants. The r_s 's are the bond vectors between atoms with equilibrium distance $r_{s,0}$; i.e., the natural In-As and Ga-As bond lengths. **Figure M-16** shows the resulting statistically-averaged In-As and Ga-As bond lengths for cubic clusters (dashed lines) and for clusters that have been tetragonally distorted in accordance with Eq. 1 (solid lines). The results of the calculation are in excellent agreement with the bulk measurements of Mikkelsen and Boyce^[3] and the results of the present study, thereby confirming the uniform nature of the bond-length distortion. ■

- [1] L.D. Landau and E.M. Lifshitz, *Theory of Elasticity* (Pergamon Press, Oxford, 1970).
- [2] J.C. Woicik, J.G. Pellegrino, B. Steiner, K.E. Miyano, S.G. Bompadre, L.B. Sorensen, T.-L. Lee, and S. Khalid, *Phys. Rev. Lett.* **79**, 5026 (1997).
- [3] J.C. Mikkelsen, Jr. and J.B. Boyce, *Phys. Rev. Lett.* **49**, 1412 (1982).
- [4] J. Hornstra and W.J. Bartels, *J. Cryst. Growth* **44**, 513 (1978).
- [5] J.C. Woicik, *Phys. Rev. B* **57**, 1 (1998).
- [6] P.N. Keating, *Phys. Rev.* **145**, 637 (1966).